# Effects of misalignments on the static and dynamic behaviour of a multiple overconstrained compliant 4-bar mechanism

van de Sande, Werner W.P.J.; Aarts, Ronald G.K.M.; Brouwer, Dannis M.

**DOI**
10.1016/j.precisioneng.2019.06.010

**Publication date**
2019

**Document Version**
Final published version

**Published in**
Precision Engineering

Precision Engineering 60 (2019) 143–151

Contents lists available at ScienceDirect

Precision Engineering

journal homepage: www.elsevier.com/locate/precision

# Effects of misalignments on the static and dynamic behaviour of a multiple overconstrained compliant 4-bar mechanism

Werner W.P.J. van de Sande[a,*], Ronald G.K.M. Aarts[b], Dannis M. Brouwer[c]

[a] Mechatronic System Design, Department of Precision Microsystems Engineering, Faculty of Mechanical, Maritime and Materials Engineering, Delft University of Technology, Delft, the Netherlands
[b] Structural Dynamics, Acoustics and Control, Department of Mechanics of Solids, Surfaces and Systems, University of Twente, Enschede, the Netherlands
[c] Precision Engineering, Department of Mechanics of Solids, Surfaces and Systems, University of Twente, Enschede, the Netherlands

A B S T R A C T

The use of overconstrained mechanisms is often avoided in precision mechanics. Misalignments in the mechanism can cause deteriorated system behaviour, such as buckling. Overconstrained designs do have several advantages, such as higher load bearing capacity and higher natural frequencies. However, these advantages are only present if the mechanism is aligned within certain tolerances. In this paper a method is introduced to identify the limits of these alignment tolerances. The method allows the calculation of the forces in the mechanism due to misalignment. The internal forces are compared to the buckling loads of the mechanism yielding the critical misalignments; the method is corroborated using a multibody simulations. Subsequently, both analyses are compared to an experimental setup; this setup measures the first three modal frequencies and identifies the buckling modes. The proposed method and multibody simulation match with each other and the experiment. However, the critical misalignments are about 20% larger in the experiment; this is mainly attributed to hardware imperfections. Due to misalignment and flatness limitations of the flexures, the undeflected stiffness in the experiment is lower than modelled. The deterioration of the support stiffness is smaller in the experiment. In the most serious case, it retains 80% of the modal frequency in the support directions. The proposed method can be used as a guideline to estimate the manufacturing and assembly tolerances of an overconstrained flexure-based mechanism.

## 1. Introduction

Compliant mechanisms are known for their predictable behaviour, no backlash, low hysteresis and no friction, which is why they are used in precision mechanics [1–10].

A second principle often used in precision mechanisms is the use of exact constraint design, which ensures a mechanism has exactly the right amount of constraint (stiff) and free (compliant) directions. However, this principle has some drawbacks such as limited load carrying capability, limited support stiffness, asymmetry, often complex design and high stress concentrations at the attachments [11].

Overconstrained designs do not suffer from these drawbacks, but are sensitive to misalignments due to assembly, fabrication tolerances and asymmetric expansion due to heat sources. Misalignment causes internal stress which will cause unwanted static and dynamic system behaviour, such as buckling and deteriorated support stiffness [8,9,11,12].

The consequences of misalignment on a once-overconstrained parallel leaf spring guidance have been investigated by Meijaard et al. [11]; a small misalignment in the overconstrained direction caused significant changes in the static and dynamic system behaviour. It especially showed a strong decrease in stiffness in the supporting directions; which is particularly disturbing for the use in precision mechanisms. However, when the misalignment was kept below 50% of the buckling angle, the stiffness of the mechanism was not influenced significantly.

Nijenhuis et al. concluded that for a cross flexure with one overconstraint the critical misalignment level is considerably larger in practice than the idealized theoretical value. Practical mechanisms seem more tolerant to misalignment errors than the ideal bifurcation buckling load suggests, due to extra sources of compliance that are present [12].

This article investigates the effects of overconstraints on an entire mechanism opposed to the effects of overconstraints on a single compliant joint. Specifically the effects of misalignments on a compliant 4-bar mechanism is investigated. This mechanism only has overconstraints on the mechanism level; the compliant joints are exact constrained.

As such, the work outlined in this article can be used as a guideline to estimate the manufacturing and assembly tolerances of an overconstrained flexure-based mechanism. The proposed method determines the critical misalignments of a flexure-based mechanism and thus the range of pre-buckling behaviour. The range of pre-buckling behaviour of a three times overconstrained compliant 4-bar mechanism

* Corresponding author.
*E-mail address:* w.w.p.j.vandesande@tudelft.nl (W.W.P.J. van de Sande).

https://doi.org/10.1016/j.precisioneng.2019.06.010
Received 18 January 2019; Received in revised form 27 May 2019; Accepted 19 June 2019
Available online 02 August 2019
0141-6359/ 

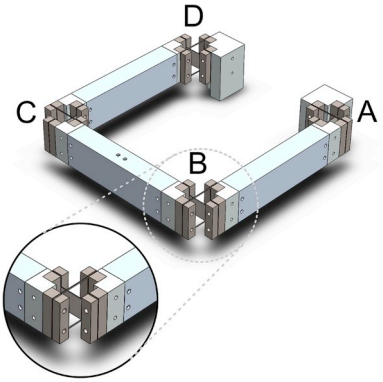


**Fig. 1.** Overconstrained 4-bar mechanism with exactly constrained cross pivot flexures as hinges.

is determined. The sensitivity for misalignment on the system behaviour in each of the overconstrained directions is analysed. The proposed method is corroborated against a multibody simulation to compare the obtained critical misalignments. These approaches are then validated with a measurement setup. The relation between the change in stiffness and the critical misalignment is also investigated. This will reveal any significant change in the dynamic behaviour. The limits of the optimal stiffness behaviour is also denoted by this change in dynamic behaviour.

In section 2 the 4-bar mechanism and measurement setup are introduced that will be used to investigate the effects of multiple overconstraints. In section 3 the proposed method for estimating the critical misalignments is introduced. Section 4 compares the buckling method results with numerical models and the results of the experiment. The experiment also contains a modal analysis to analyse the dynamic effects of the misalignments. The work concludes with a discussion and a conclusion on the results.

## 2. System description

The 4-bar mechanism under consideration is shown in Fig. 1. The rigid bars are connected by four compliant hinges. These four hinges are equal in dimension, but different in orientation. Hinges A and C have the same orientation and hinges B and D are rotated 90° relative to hinges A and C. The flexure hinges must behave as exact constraint revolute joints in order for the compliant 4-bar mechanism to have the same amount of constraints as its kinematic equivalent. The resulting compliant 4-bar mechanism has one degree of freedom (DOF) and 3 overconstraints.

### 2.1. System kinematics

A 4-bar mechanism consists of four links and four revolute joints. The mobility of a 4 bar mechanism can be determined with Grübler's equation [13]. In the 2D analysis it has 1 DOF; in the 3D analysis it has −2 DOF. It appears that in 3D the 4-bar mechanism has negative mobility. The result of Grübler's equation in 3D case can be considered as the sum of the mobility ("underconstraints") and overconstraints; a planar 4-bar mechanism has one DOF and therefore must also have three overconstraints [14]. However, Grübler's equation does not list in which directions the mobility and overconstraints are.

A way to investigate this is to open the loop and deduce the mobility and overconstraints. The kinematic loop can be opened at one of the hinges as seen in Fig. 2.

The left chain consists of two revolute joints and two links; the right chain consists of two revolute joints and one rigid link, both chains have two DOFs.

As seen in Fig. 2, the left chain has the following freedoms and constraints.

$$\mathbf{f_l} = \{t_x \quad t_y\};\ \mathbf{c_l} = \{f_z \quad m_x \quad m_y \quad m_z\} \tag{1}$$

The freedoms are listed as movement in a direction, whereas the constraints are listed as forces and moments that prevent movement in those directions. The right chain has the following freedoms and constraints.

$$\mathbf{f_r} = \{t_x \quad r_x\};\ \mathbf{c_r} = \{f_y \quad f_z \quad m_x \quad m_y\} \tag{2}$$

Here the freedoms are expressed as $\mathbf{f_l}$ and $\mathbf{f_r}$ for the left and right chains respectively. The directions are the translations $t_x$, $t_y$ and $t_z$, while the rotations around these axes are expressed by $r_x$, $r_y$ and $r_z$ respectively.

The constraints are expressed as $\mathbf{c_l}$ and $\mathbf{c_r}$. There are three forces: $f_x$, $f_y$ and $f_z$, that constrain translations in those directions; there are also three moments: $m_x$, $m_y$ and $m_z$.

The total mobility of the mechanism is determined by the intersection of the mobility of the chains [15]:

$$M = \mathbf{f_l} \cap \mathbf{f_r} = \{t_x\} \tag{3}$$

In the case of a planar parallel 4-bar mechanism this is the translation in the $x$-direction.

The constraints of the mechanism are determined by the span of the constraints of the chains.

$$C = \{\mathbf{c_l} \quad \mathbf{c_r}\} = \{f_y \quad f_z \quad m_x \quad m_y \quad m_z\} \tag{4}$$

The three overconstraints can be obtained by the intersection of the constraints of the left and right chain.

$$O = \mathbf{c_l} \cap \mathbf{c_r} = \{f_z \quad m_x \quad m_y\} \tag{5}$$

These three overconstraints are in the out-of-plane directions, which are $z$, $\varphi$ and $\psi$ directions for the $f_z$, $m_x$ and $m_y$ constraints respectively (see Fig. 2). This corresponds with the results of Grübler's equation, where the overconstraints only manifest in the spatial case.

Exact constraint compliant hinges are needed to achieve the same amount of overconstraints in the compliant 4-bar mechanism. This is done by placing two wire parallel flexures perpendicular to a leaf spring. The wire flexures are offset from each other. Each wire-flexure constrain 1 DOF and the leaf spring constrain 3 DOFs. All constraints are applied independently; i.e. no constraint can be expressed as a combination of the other constraints. This leads to 5 constraints in total. The resulting flexure hinge has no overconstraints and one compliant rotation.

### 2.2. System dimensions and properties

The length of the leaf spring and the wire flexures in the hinges are both $l_h$. The thickness and height of the leaf spring are $t_{lf}$ and $b_{lf}$ respectively; the wire flexures have a thickness $t_{wf}$ and a height $b_{wf}$. The wire flexures are a distance $d_{wf}$ apart. The rigid bars are of length $l_b$ so that the centres of the hinges are $L$ apart. The values used for these variables can be seen in Table 1.

The flexures are made from stainless spring steel (EN 1.4310) that is laser-cut from a larger sheet. These are clamped with steel blocks to the aluminium bars. The material properties of all components of the mechanism are shown in Table 2.

The elastic properties of the bars are not considered; the masses and moments of inertia of the bars are. The mass of a bar is the lumped mass of all the steel blocks and aluminium components between two hinges; the mass properties (masses/moments of inertia/centre of mass) can be seen in Table 3. The axes are in the global mechanism coordinate system (Fig. 2); the origin is at the centre of hinge A. All non-mentioned parameters are zero; the data is obtained using a CAD program.

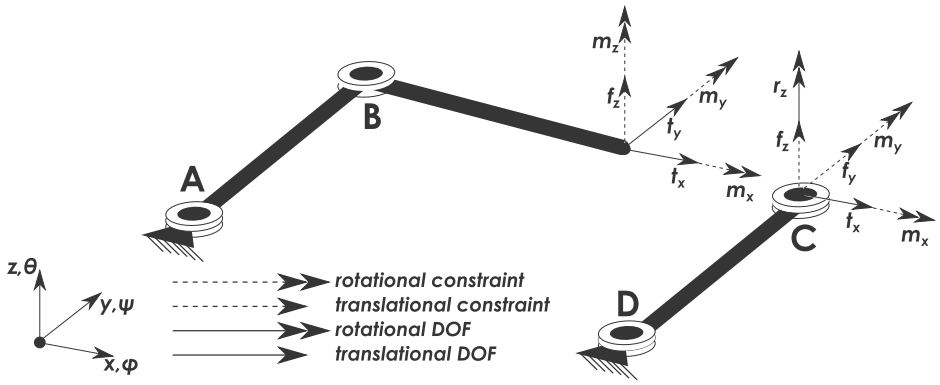


**Fig. 2.** The kinematics of a 4-bar mechanism illustrated by opening the loop at hinge C.

**Table 1**
Dimensions of the components in the mechanism.

| Variable | $l_h$ | $t_{lf}$ | $b_{lf}$ | $t_{wf}$ | $b_{wf}$ | $d_{wf}$ | $l_b$ | $L$ |
|---|---|---|---|---|---|---|---|---|
| value (mm) | 30 | 0.5 | 19.7 | 0.7 | 0.8 | 39 | 170 | 200 |

**Table 2**
Material properties of the components in the mechanism.

| Property | unit | spring steel | steel | aluminium |
|---|---|---|---|---|
| ρ | kg/m$^3$ | 8000 | 7800 | 2800 |
| $E$ | GPa | 200 | 200 | 70 |
| $\nu$ | – | 0.3 | 0.3 | 0.3 |

**Table 3**
Mass properties of the bars.

| Bar | left | effector | right |
|---|---|---|---|
| $m$(kg) | 0.48 | 0.58 | 0.48 |
| $J_{xx}$(kgm$^2$) | $2.81{\cdot}10^{-3}$ | $4.65{\cdot}10^{-4}$ | $2.81{\cdot}10^{-3}$ |
| $J_{yy}$(kgm$^2$) | $1.11{\cdot}10^{-4}$ | $3.18{\cdot}10^{-3}$ | $1.11{\cdot}10^{-4}$ |
| $J_{yz}$(kgm$^2$) | 0 | $2.58{\cdot}10^{-6}$ | 0 |
| $J_{zz}$(kgm$^2$) | $2.79{\cdot}10^{-3}$ | $2.81{\cdot}10^{-3}$ | $2.79{\cdot}10^{-3}$ |
| $x_c$(mm) | −12.1 | 100 | 212.1 |
| $y_c$(mm) | 100 | 212.1 | 100 |
| $z_c$(mm) | 0 | 9.28 | 0 |

### 2.3. Description of test setup and equipment

An overview of the experimental setup is shown in Fig. 3. There are four exactly constrained cross pivot flexures (Fig. 3 A through D). At point D a manipulator connects the mechanism to the fixed world. The manipulator enables adjustment of the 3 overconstrained directions of the mechanism. It can be adjusted to result in a near stress-free 4 bar overconstrained mechanism. The three arms of the manipulator are placed 120° apart. These are constrained by three folded sheet flexures Fig. 3 G); The flexures constrain the movement in the in-plane directions ($x$, $y$ and $\theta$), but leave the overconstrained directions of the mechanism free. The goal is to be able to precisely align or misalign the overconstrained directions in order to observe the change in behaviour of the mechanism. The height of each of the three arms can be set by a screw (Fig. 3H); the arms are preloaded against the screws with three helical springs. The preload ensures contact with the screws; this eliminates play in the positioning of the manipulator. It also increases the stiffness of the connection between the ground and the manipulator in the overconstrained directions. The height of the arms is measured by three dial gauges (Fig. 3 E).

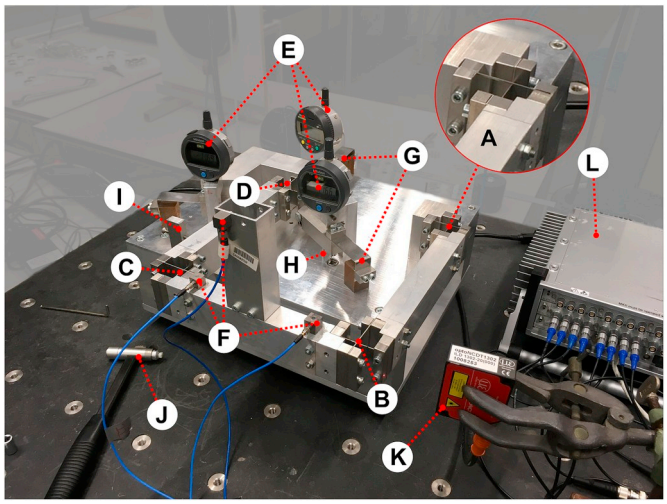


**Fig. 3.** Overview of the experimental setup.

The vibrations of the end-effector are measured using three accelerometers (Fig. 3 F). The acceleration is measured at three positions: at two locations next to hinges at the end of the end-effector facing downwards and one at the top of the inverted T facing towards the manipulator.

The end-effector is excited using a modal hammer (Fig. 3 J); the force was applied next to one of the downward facing accelerometers (Fig. 3C and F). The data is processed in a Mueller-BBM Pak Mk II system (Fig. 3 L). The compliant mode is measured using a laser displacement sensor (Fig. 3 K); to avoid non-linear effects the compliant mode is positioned against a stop (Fig. 3 I) to ensure repeatable amplitudes at every measurement. The buckling of the flexures is observed visually.

## 3. Method

The critical values and shapes of buckling are identified in a compliant 4-bar mechanism with exact constraint cross pivot flexures. We introduce a method that will obtain a relation between misalignments and the resultant loads in the mechanism. These resultant loads are compared to the buckling scenarios.

### 3.1. Buckling scenarios of a compliant 4-bar mechanism

In the compliant 4-bar mechanism only the cross pivot flexures are prone to buckling. In this compliant hinge there are two distinct buckling modes: axial buckling of a wire flexure and lateral buckling of the leaf spring flexure. The hinge is assumed to be in its neutral position and will stay in or near its neutral position when buckling.

Lateral buckling of a leaf spring can occur due to a force in the direction of the height of the flexure and a moment in the plane of the flexure. The buckling loads can be determined with the classical equations outlined by Timoshenko [16].

The buckling of a leaf spring is governed by the following equations.

$$M_{cr,lf} = \frac{\gamma_1}{l}\sqrt{EI_z GJ_t}$$
$$F_{cr,lf} = \frac{\gamma_2}{l^2}\sqrt{EI_z GJ_t} \tag{6}$$

The buckling moment, $M_{cr,lf}$, and the buckling force $F_{cr,lf}$ are dependent material properties: the Young's Modulus, $E$ and the modulus of rigidity, $G$. The following geometric properties also influence the buckling loads: the second moment of area, $I_z$, and the torsional constant $J_t$ and the length of the flexure $l$. The buckling moment and force are corrected with the parameters $\gamma_1$ and $\gamma_2$ respectively. These parameters are influenced by the constraints of the leaf spring, such as the elastic boundary conditions and warping constraints.

Likewise the buckling of a wire flexure due to an axial force is as follows.

$$F_{cr,wf} = \frac{\gamma_3}{l^2}EI_z \tag{7}$$

The correcting factor, $\gamma_3$, is only dependent on the boundary conditions. There are two parallel wire flexures in the hinge. A moment in the plane of these flexures will yield an axial load on both wire flexures.

$$M_{cr,wf} = d\frac{\gamma_3}{l^2}EI_z \tag{8}$$

In which $M_{cr,wf}$ is the critical buckling moment and $d$ the distance between the flexures. The cross pivot flexure has three distinct buckling scenarios that correspond with the overconstrained directions: a force in the $z$-direction in the mechanism coordinate system and two moments perpendicular to each other and the $z$-direction.

### 3.2. Hinge compliance

As a first step, an expression for the lumped compliance of the hinges has to be found. In this parallel configuration of the cross pivot flexure, the stiffness of the flexure is the sum of the stiffness contributions of the leaf spring and the wire flexures. The flexure is designed such that the centres of compliance of the leaf spring and wire flexures overlap. The centre of compliance is the point in certain flexures where a force or moment in a certain direction will only cause a displacement in that same direction [17]. This will yield a diagonal compliance matrix. Consequently, the stiffness in the centre of compliance of the cross pivot flexure is the sum of the stiffness of the leaf spring and wire flexures.

Both the leaf spring and the wire flexures are made of the same material. Using the geometric properties outlined in the previous section and the well-known formulas the stiffness in the centre of compliance of the leaf spring and wire flexure are determined [17,18]. These expressions are valid for small deflections.

$$\boldsymbol{K}_{lf} = diag\left(\frac{Eb_{lf}t_{lf}^3}{l_h^3} \quad \frac{\mathbf{Eb_{lf}t_{lf}}}{\mathbf{l_h}} \quad \frac{\mathbf{Et_{lf}b_{lf}^3}}{\mathbf{l_h^3}} \quad \frac{\mathbf{Et_{lf}b_{lf}^3}}{\mathbf{12l_h}} \quad \frac{GJ_{t,lf}}{l_h} \quad \frac{\mathbf{Eb_{lf}t_{lf}^3}}{\mathbf{12l_h}}\right) \tag{9}$$

$$\boldsymbol{K}_{wf} = diag\left(\mathbf{2\frac{Eb_{wf}t_{wf}}{l_h}} \quad 2\frac{Eb_{wf}t_{wf}^3}{l_h^3} \quad 2\frac{Et_{wf}b_{wf}^3}{l_h^3} \quad 2\frac{GJ_{t,wf}}{l_h} + 2\frac{Eb_{wf}t_{wf}^3}{l_h^3}d_{wf}^2 \quad \frac{\boldsymbol{Eb_{wf}t_{wf}}}{\boldsymbol{l_h}}\boldsymbol{d_{wf}^2} \quad \mathbf{2\frac{Eb_{wf}t_{wf}^3}{12l_h}}\right) \tag{10}$$

The stiffness matrix of the leaf spring is expressed as $K_{lf}$ and the stiffness matrix of the pair of wire flexures is defined as $K_{wf}$. The torsional constants $J_{t,lf}$ and $J_{t,wf}$ are derived from the dimensions of the cross sections. In all directions, except the compliant rotation around the $z$-axis, one of the flexures is dominant in stiffness. The dominant stiffness contributions are listed in bold in equations (9) and (10). The hinge stiffness is approximated by neglecting the relative small terms in the sum.

$$\boldsymbol{K}_h \approx diag\left(2\frac{Eb_{wf}t_{wf}}{l_h} \quad \frac{Eb_{lf}t_{lf}}{l_h} \quad \frac{Et_{lf}b_{lf}^3}{l_h^3} \quad \frac{Et_{lf}b_{lf}^3}{12l_h} \quad \frac{Eb_{wf}t_{wf}}{l_h}d_{wf}^2 \quad \frac{Eb_{lf}t_{lf}^3}{12l_h} + 2\frac{Eb_{wf}t_{wf}^3}{12l_h}\right) \tag{11}$$

The stiffness matrix of a hinge $\boldsymbol{K}_h$ is inverted to obtain the hinge compliance matrix $\boldsymbol{C}_\mathbf{h}$.

## 4. Equivalent compliance of a serial chain

The misalignments are applied at the manipulator at the centre of compliance of hinge D. The relation between a misalignment and the resultant loads at hinge D is expressed by the stiffness of the mechanism at hinge D. The 4-bar mechanism is connected at the world at hinge A. It can be expressed as a serial chain of links and hinges towards hinge D; therefore the compliance of all hinges can be added together.

$${}^{(M)}C_{total} = \sum_{i=1}^{n} H_{i,(M)}\,{}^{(i)}CH_{i,(M)}^T \tag{12}$$

The compliance of each hinge is expressed in its local reference frame. As such, the compliance of each hinge $i$ has to be transformed to the mechanism reference frame, $(M)$. This can be achieved by the transformation matrix $H$; $H$ is a 6 by 6 transformation matrix. The transformation matrix is made up out of a 3 by 3 rotation matrix $R$ and a 3 by 3 matrix $T$. The matrix $T$ is the skew-symmetric, or cross-product, matrix of a 3 by 1 translation vector $t$ [19].

$$H = \begin{bmatrix} R & TR \\ 0 & R \end{bmatrix} \tag{13}$$

The matrix $H$ is in this shape since the compliance matrix transforms loads into displacements. Moments and translations are invariant under translation of a coordinate system. In a load vector the moments are at the bottom, whereas in a displacement vector the translations are at the top. The transformation matrix $H$ is also used to transform displacement vectors.

For load vectors and the stiffness matrix the transformation matrix is different.

$$A = \begin{bmatrix} R & 0 \\ TR & R \end{bmatrix} = H^{-T} \tag{14}$$

The transformation matrices are dependent on the pose of the mechanism. For simplicity it is assumed that is adequate enough for small deflections.

### 4.1. Critical misalignments of the overconstrained compliant 4-bar mechanism

The contents of the previous sub-sections are used to obtain the critical misalignments.

The compliances of the hinges are added together to get the compliance at the manipulator using equation (12). The transformations are from the centre of compliance at each hinge to the centre of compliance of hinge D. The centre of compliance of each hinge has specific coordinates with respect to the manipulator.

$$t_A = \{-L \;\; 0 \;\; 0\}^T;\; t_B = \{-L \;\; L \;\; 0\}^T;\; t_C = \{0 \;\; L \;\; 0\}^T;\; t_D = \{0 \;\; 0 \;\; 0\}^T \tag{15}$$

In this specific arrangement of hinges, hinges B and D are rotated 90° with respect to the global coordinate system (see Fig. 2).

The sum of all these matrices is the equivalent compliance at the manipulator at hinge D.

The lengths between the centres of compliances of the hinges is $L$. The terms $s_a$, $s_b$, $s_c$, $s_\alpha$, $s_\beta$ and $s_\gamma$ are the cardinal compliances of the hinge; these are the inverse of the terms found in equation (11). The

$$
{}^{(M)}C_D = \sum_{j=1}^{n} {}^{(M)}C_i
$$

$$
= \begin{bmatrix}
2s_\gamma L^2 + 2s_a + 2s_b & s_\gamma L^2 & 0 & 0 & 0 & 2s_\gamma L \\
s_\gamma L^2 & 2s_\gamma L^2 + 2s_a + 2s_b & 0 & 0 & 0 & 2s_\gamma L \\
0 & 0 & \mathbf{4s_c + 2s_\alpha L^2 + 2s_\beta L^2} & \mathbf{-L(s_\alpha L + s_\beta)} & \mathbf{-L(s_\alpha L + s_\beta)} & 0 \\
0 & 0 & \mathbf{-L(s_\alpha L + s_\beta)} & \mathbf{2s_\alpha + 2s_\beta} & \mathbf{0} & 0 \\
0 & 0 & \mathbf{-L(s_\alpha L + s_\beta)} & \mathbf{0} & \mathbf{2s_\alpha + 2s_\beta} & 0 \\
2s_\gamma L & 2s_\gamma L & 0 & 0 & 0 & 4s_\gamma
\end{bmatrix} \tag{16}
$$

compliance of the overconstrained directions (columns 3 through 5 in equation (16)) is decoupled from the compliance in the in plane directions. This submatrix is inverted to obtain the equivalent stiffness matrix.

With the overconstraint stiffness matrix we can obtain the resultant loads in the overconstrained directions at the manipulator as a result of a chosen misalignment. These are chosen to be $1mm$ in the $z$ direction and $1mrad$ in the $\varphi$ and $\psi$ directions. This misalignment is written as a 3 by 1 displacement vector. The resultant load vectors at the hinges are determined using the transformation matrix from the manipulator to the hinge.

$$\lambda_{ij} = A_{m,j}\ {}^{(m)}K\delta_i \tag{17}$$

In which $\lambda_{ij}$ is a load due to a misalignment $\delta$ in the direction of $i$ at hinge $j$. The transformation matrix $A_{mj}$ determines the load at hinge $j$ due to a load at the manipulator $m$. The load at the manipulator is determined with the overconstraint stiffness matrix at the manipulator ${}^{(m)}K$ and the misalignment in the direction of $i$ at the manipulator. This results in 12 unique load cases: one for any of the four hinges due one of the three misalignments. Each of the twelve unique load cases is compared to each of the three buckling scenarios. These buckling scenarios are the buckling of a wire flexure due a moment in the plane of the two wire flexures, lateral buckling of the leaf spring flexure due to a moment in the plane of the leaf spring flexure or a force in the lateral direction of the leaf spring. These buckling loads are expressed by the parameter $p_k$; the values can be obtained via equations (6) and (8). The buckling multipliers are defined as the ratio between the buckling scenarios and the resultant loads $\lambda_{ij}$.

$$c_{ijk} = \frac{p_k}{\lambda_{ij}} \tag{18}$$

This buckling multiplier, $c$, indicates how many times the resultant load to a chosen misalignment needs to be applied before buckling occurs. Only one instance of buckling will occur: the one with the lowest buckling multiplier. The critical misalignment is the product of the lowest multiplier and the chosen misalignment, $\delta$. For each type of misalignment there will be one critical misalignment per hinge. The lowest critical misalignment for each type of misalignment will determine which hinge will buckle first; this is also the buckling mode for the mechanism due to that specific misalignment.

## 5. Comparison and validation

### 5.1. Buckling of the hinge

The buckling loads of the cross pivot hinge were obtained using the program SPACAR [20]; this was done since simulations could better ascertain the boundary condition of the buckling problem. In these simulations constrained warping was considered [21]. Also, rotational stiffness was added in the direction of the DOF of the hinge; this must be added to account for the stiffness of the other hinges as all hinges must deflect the same amount. The simulation solves these equations for a single hinge. Table 4 shows the values for all three buckling scenarios. The buckling load of the wire flexures is lower than that of the leaf spring flexure.

With the help of eq:comptot,eq:resload,eq:bumu and the geometrical and material properties of the mechanism, the buckling multipliers can be determined. Only the lowest multipliers of the twelve load cases are listed in Table 5; the lowest buckling multiplier for each hinge is listed in bold. In the case of a $z$-misalignment there is no preference in which hinge buckles first. In the $\varphi$- and $\psi$-misalignment this would be hinge D and C respectively. The orientations of the hinges ensure that in every case the wire flexures buckle.

### 5.2. Simulation results

The method is checked against a full multibody simulation, also done in the software SPACAR. Gravity is not considered, but constrained warping is. The critical misalignments can be seen in Table 6. The values for the method were obtained by taking the lowest buckling multipliers for each hinge and multiplying them with the corresponding unit misalignment.

The mechanism simulation shows overall lower values for the critical buckling multipliers when compared to the method. In the case of the $\varphi$- and $\psi$-misalignments it is about 96% of the estimated analytical buckling multiplier. The $z$-direction is different; the multibody analysis is about 80% of the amount predicted by the analytical model. The buckling modes are consistent with the prediction of the method. For instance, it can be seen in Table 5 that in case of a $\varphi$-misalignment a

**Table 4**
Buckling loads obtained using simulation; the leaf spring flexure ($lf$) buckles due to lateral loads, whereas the wire flexures ($wf$) buckle due to axial loads.

| | lateral buckling | axial buckling |
|---|---|---|
| $F_{lf}$ (N) | $2.22{\cdot}10^3$ | – |
| $M_{lf}$ (Nm) | 10.39 | – |
| $M_{wf}$ (Nm) | – | 8.40 |

**Table 5**
The buckling multipliers of the hinges determined with the method; the buckling scenario is listed (w) for wire flexures and (l) for leaf spring flexures. The lowest buckling multipliers per misalignment are shown in bold.

| Misalignment | hinge A | hinge B | hinge C | hinge D |
|---|---|---|---|---|
| $z$ | **2.64** (w) | **2.64** (w) | **2.64** (w) | **2.64** (w) |
| $\varphi$ | 10.87 (l) | 26.20 (w) | 26.43 (w) | **8.79** (w) |
| $\psi$ | 26.20 (w) | 26.43 (w) | **8.79** (w) | 10.87 (l) |

**Table 6**
The derived and simulated critical misalignments of the mechanism without gravity.

| Misalignment | $z(mm)$ | $\varphi(mrad)$ | $\psi(mrad)$ |
|---|---|---|---|
| mechanism simulation | 2.10 | 8.48 | 8.48 |
| method | 2.64 | 8.79 | 8.79 |

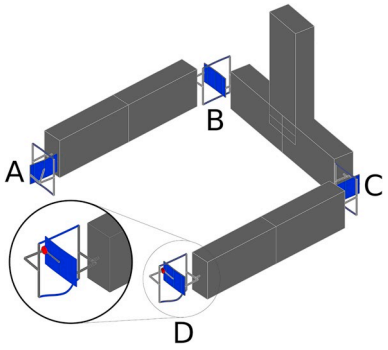


**Fig. 4.** Buckling of hinge D due to a $\varphi$-misalignment.

wire flexure of hinge D buckles first; the mechanism simulation also shows this behaviour (Fig. 4).

### 5.3. Experimental results

An experiment was conducted to validate the results of the method and the multibody simulation. An additional multibody simulation is done up to account for gravity; this is done to accurately compare to the conditions in the experiment. The experiment and the new simulation with gravity are compared to the multibody simulation without gravity and the method. The simulations and experiment also contain modal data. Three rigid body modes of the end-effector are compared, see Fig. 5. The first mode is the mode of the DOF of the mechanism, which is in the $x$-direction (see coordinate system Fig. 2). The second mode is the $z$-motion of the end-effector, whereas the third modes is the $\psi$-motion of the end-effector. These three modes are compared for all three types of misalignments. The misalignments are varied using the manipulator; it is increased until visible buckling was observed. The modes are measured using the accelerometers. The data is transformed to the frequency domain to obtain the modal frequencies and phases. This is done by the PAK software that comes with the Müller-BBM PAK MkII measurement system. The frequencies and the phase of the data were used to identify the mode shapes. For instance, for the second mode the outermost accelerometers are in phase with one another. Whereas for the third mode these are in counter phase.

In the simulations the flexures were pre-curved with half the thickness of the leaf spring. In Fig. 6 the effect of pre-curving can be seen; without pre-curving the flexures there is an abrupt change in frequency near the critical misalignment. In the experiment the deterioration is much more gradual. As such, the value of half the leaf

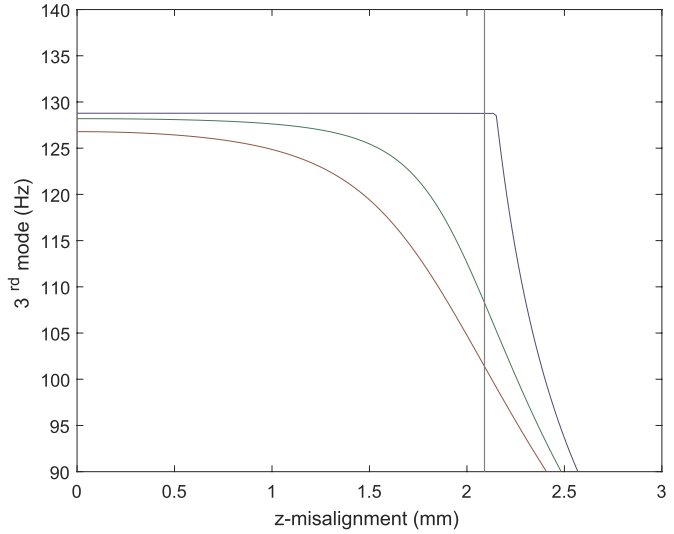


**Fig. 6.** Effects of a precurve of the flexures on the dynamic behaviour of the mechanism blue: no precurve green: precurve of half the leaf spring thickness (0.25 mm) red: precurve of a single leaf spring thickness (0.5 mm) grey: critical misalignment in simulation. (For interpretation of the references to colour in this figure legend, the reader is referred to the Web version of this article.)

spring thickness was chosen to ensure a gradual frequency deterioration as seen in the experiment. This value is also small enough to assume that the mechanism is in the neutral position.

The results of the simulations and experiment can be seen in Figs. 7–9 for the $z$-, $\varphi$- and $\psi$-misalignments respectively. The critical misalignments are indicated by vertical lines. The experimental data is shown in black. It was fitted on the measurement points which are shown as open circles. The simulation without and with gravity are shown in red and green respectively.

There is no real difference between the simulations in the case of $\psi$-misalignment. This is different when it comes to misalignment in the $\varphi$-direction. A wire flexure of hinge D buckles; the location and orientation of that wire flexure plays a large role in the support of the mechanism (see Fig. 6). This can be seen in the change of the second mode (Fig. 8). The resurgence of the first mode after buckling in the simulations was also observed in the experiment. The asymetry of the first mode due to $\varphi$-misalignment in the simulation with gravity was also observed. There is also an asymetry due to $\psi$-misalignment which was not displayed in the simulations. The change in frequency of the first mode from zero misalignment to the critical misalignment is about 0.35 Hz.

The critical misalignments values found in the experiments exceed those of the simulations and the method. This can be hard to see in the figures due to difference in alignment between the experiment and simulations. Table 7 lists the distance between the positive and the negative misalignments for better comparison.

The experiment exceeds both simulations by about 20%. This difference can be partly explained by the fact that the simulations display

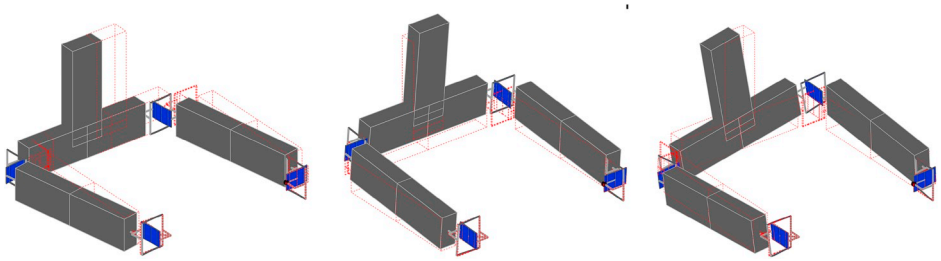

**Fig. 5.** Modal shapes of the first three modes, from left to right: the $x$-motion of the first mode, the $z$-motion of the second mode and the $\psi$-motion of the third mode.

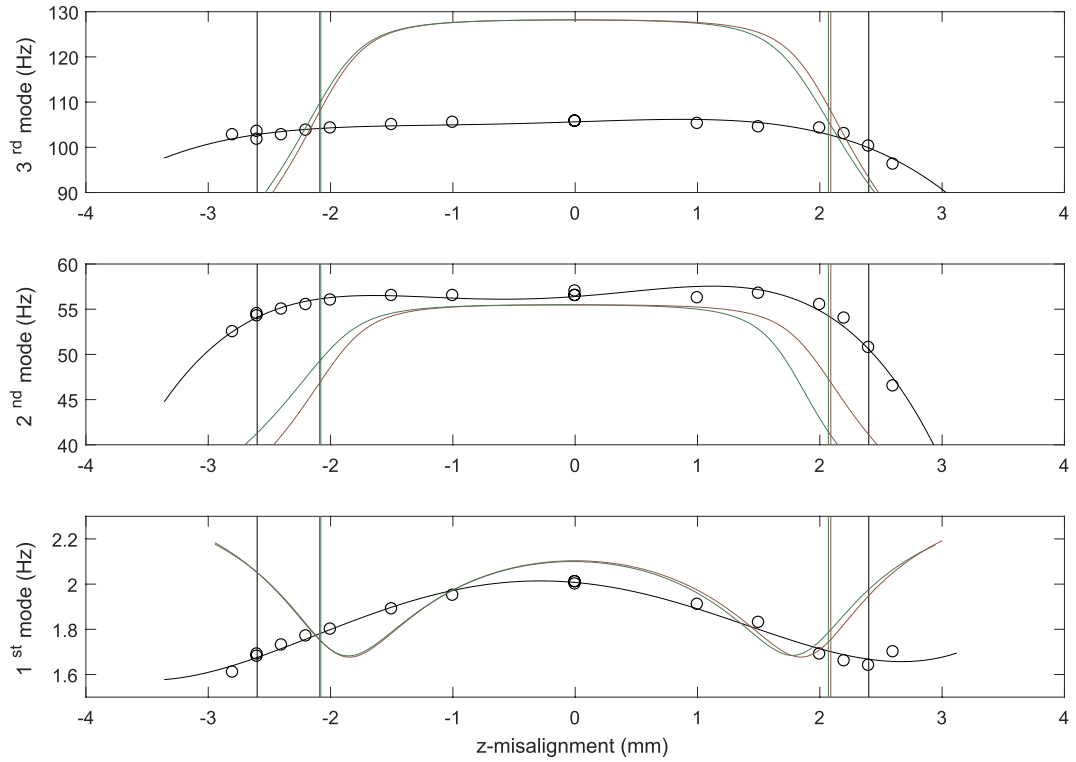


**Fig. 7.** Change in three modes due to a misalignment in the $z$-direction vertical lines denotes the critical misalignment red: simulation without gravitygreen simulation with gravity black: experimental data (fitted with data points as circles). (For interpretation of the references to colour in this figure legend, the reader is referred to the Web version of this article.)

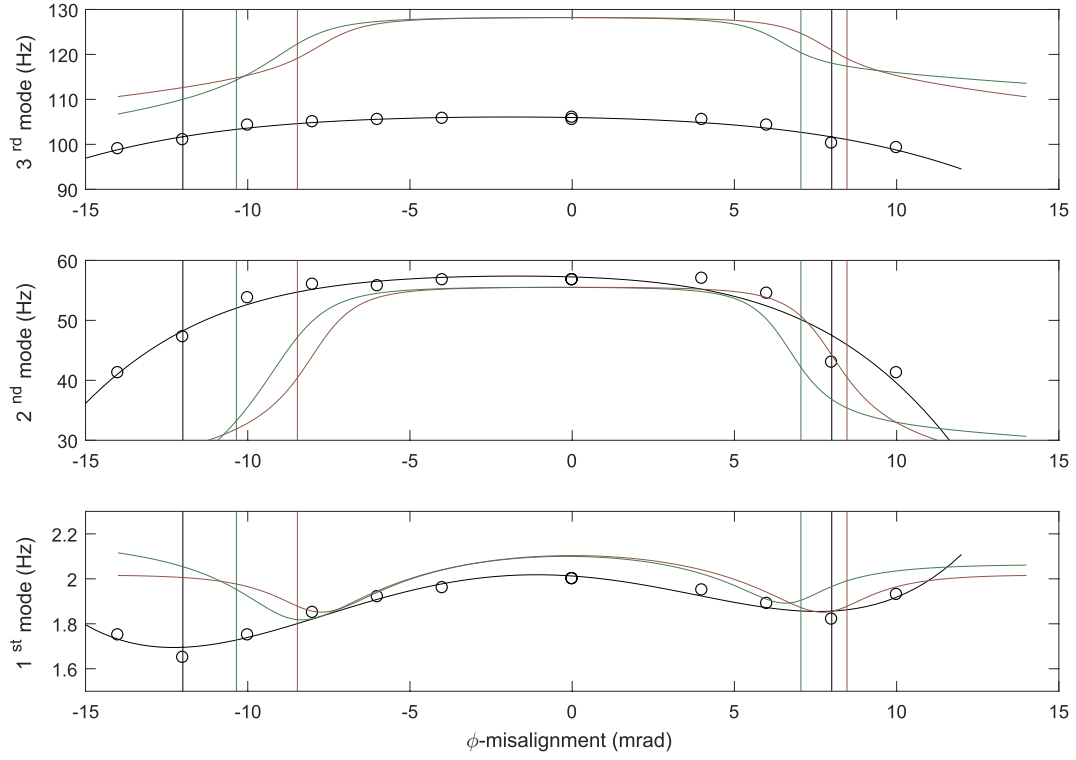


**Fig. 8.** Change in three modes due to a misalignment in the $\varphi$-direction vertical lines denotes the critical misalignment red: simulation without gravity green: simulation with gravity black: experimental data (fitted with data points as circles). (For interpretation of the references to colour in this figure legend, the reader is referred to the Web version of this article.)

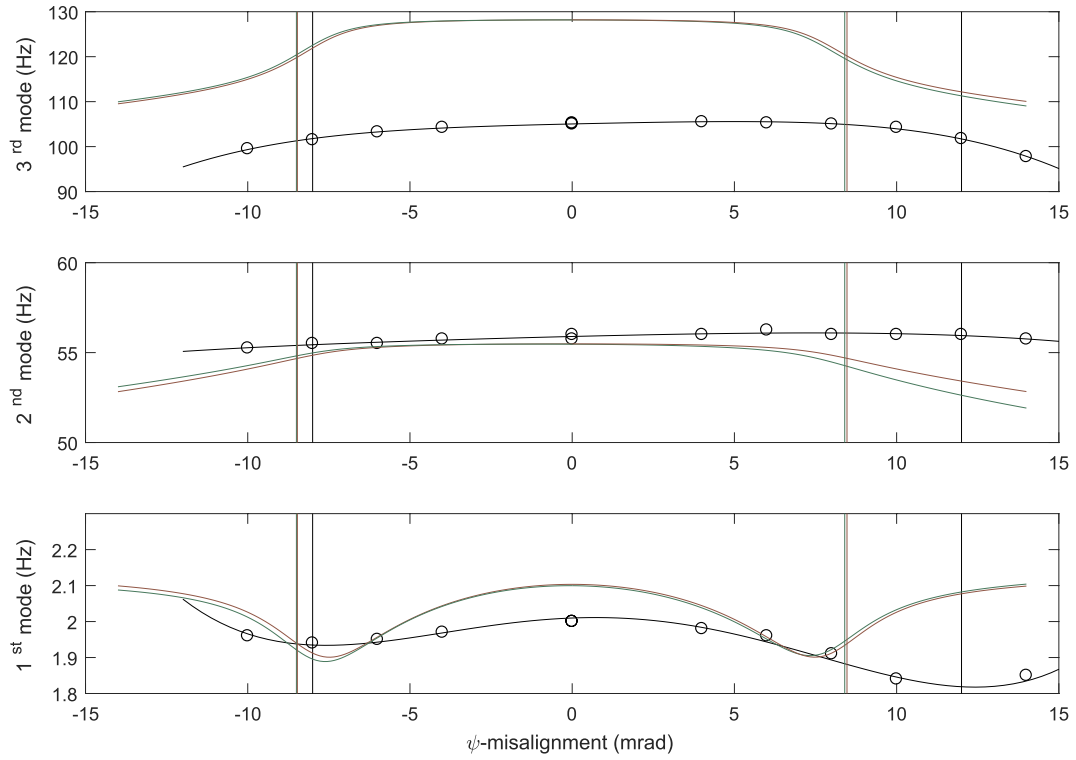


**Fig. 9.** Change in three modes due to a misalignment in the $\psi$-direction vertical lines denotes the critical misalignment red: simulation without gravity green: simulation with gravity black: experimental data (fitted with data points as circles). (For interpretation of the references to colour in this figure legend, the reader is referred to the Web version of this article.)

**Table 7**
Difference between the positive and negative critical misalignments for all three overconstrained directions (both in distance and as a percentage of the simulation without gravity).

| Total misalignment | $\Delta z(mm)$ | $\Delta\varphi(mrad)$ | $\Delta\psi(mrad)$ |
|---|---|---|---|
| simulation without gravity | 4.20 (100%) | 17.0 (100%) | 17.0 (100%) |
| simulation with gravity | 4.24 (101%) | 17.4 (103%) | 17.0 (100%) |
| experiment | 5.00 (119%) | 20.0 (118%) | 20.0 (118%) |

the theoretical buckling misalignment; the critical misalignment in the experiment was observed visually (black vertical lines in Figs. 7, 8 and 9). Observed buckling is most likely higher than theoretical buckling. The range of high frequency before it deteriorates due to internal stress is wider in the experiment. This effect cannot simply be explained by a higher observed buckling value. The deterioration of the modal frequencies in the support directions is limited. In the worst case, a $\varphi$-misalignment, the frequency of the second mode decreases by 20% at most. Other effects, such as hardware and assembly errors can also cause the higher critical misalignment. For instance, extra compliance in the flexures as well as small alignment errors in the clamping of the flexures can cause a higher critical misalignment. Other effects, such as the flatness and minor deflections of the flexures will also affect the stiffness of the mechanism.

The frequencies of the first and third modes are lower in the experiment than in the simulations. The masses of the accelerometers are taken into account in the simulations, so this is not the cause of the difference. The frequency of the second mode does not display the same behaviour; the frequency matches between the simulations and the experiment.

This difference in frequency is probably caused by hardware imperfections in the experimental setup that were not included in the numerical model. These factors can be the clamping effects of the hinges and errors in manufacturing and assembly [22].

## 6. Discussion

The buckling analysis method is a suitable method to determine the critical misalignments in a 4-bar mechanism. Although the buckling method is applicable in this specific case, it has some limitations. First, the precise buckling boundary conditions and warping constraints must be determined to calculate the buckling multipliers. This remains a difficult problem; in this article this was only done using simulation. An analytical solution is yet to be determined. Furthermore, the changes in frequency seen in the experiment indicate that the mechanism loses stiffness when approaching critical misalignment. This change influences the boundary conditions of the buckling problem, which explains the lower critical misalignment of the multibody simulation when compared to the method.

The method is able to compute the equivalent compliance of the mechanism at the manipulator as a serial linkage consisting of the hinge compliances and the rigid bars. Mechanisms can have other topologies than a pure serial chain of compliant joints. The applicability of this method in those cases is not investigated in this work. However, as long as an expression of the equivalent stiffness can be obtained the steps outlined in the method are valid. The method can also be applied to other types of flexure hinges as long as the topology does not change.

Initially the behaviour of the first mode was not much of interest since a decrease in the stiffness of the DOFs of a mechanism is considered beneficial. However, the behaviour seen in that mode proved helpful in aligning the mechanism by maximising the first mode; it also displays the effects of the misalignments really well. Further attention is still required to properly align the measurement setup.

The frequencies of the first and third mode found in the experiment are lower than those found in the simulations. This is not true for the second mode; this mode describes the up and down ($z$-direction) vibrations of the end-effector. The cause of this difference is not clear. Damping causes the natural frequencies of the mechanism to decrease. The damping was not measured; from observation it was assumed that

the damping was very low. It took several minutes for the mechanism to stop oscillating. If damping is the cause, this would indicate that the damping is also higher for the first and third modes. The second and third modes share the same type of deformations of the flexures; which seems to contradict that explanation. The different also cannot be due to inaccurate modelling of the mass or stiffness, since the other modes would be similarly affected. The only significant difference is that the second mode is in the direction of gravity; this might cause a difference in stiffness or damping.

The mechanism was designed with the explicit goal to determine the critical misalignments. Three modes were used in the analysis; the end-effector was also designed to be able to measure the modes properly. The cross pivot flexures were orientated in such a way that in any case a wire flexure would buckle; this could be easily observed in the experiment. A result of these adaptations to the basic design before conducting the experiment was helpful; these ensured that the experiment was relatively straightforward and did not require multiple design iterations.

## 7. Conclusion

The effects of misalignments on the stiffness behaviour of a compliant 4-bar mechanism with three overconstraints was investigated. A method was developed to ascertain the amount of misalignment where buckling occurs; this buckling indicates the limits of optimal stiffness behaviour in the mechanism. The method is far less complicated and time-consuming than modelling the entire mechanism in question.

The method was compared to full mechanism simulations in which the misalignment was increased until the post-buckling range was reached. The introduced method has slightly higher values for the critical misalignments than the simulation: about 25% for the z-misalignment and 3% for the other two misalignments. This is likely caused by an improper assessment of the elastic boundary conditions.

An experiment was done to validate the results of the method and simulation. A change in all three modal frequencies was observed due to all three misalignments. The same buckling modes were seen in the method and in the simulations. The values of the critical misalignments are about 20% higher than in the simulations. This result can be explained by several effects. First, buckling was visually observed, which could yield higher values than the theoretical values. In addition, several imperfections in the setup, in hardware and assembly, are likely to influence the behaviour.

The dynamic behaviour observed the simulation was compared with that observed in the experiment. It shows the same trend as the buckling comparison: a decrease of the modal frequencies is seen when the misalignments approach their critical values. In the experiment the deterioration sets in later, resulting in an increased range of optimal frequency. At worst, the modal frequency in one of the support directions drops 20% at the critical misalignment. The frequencies are generally lower in the experimental setup than in the simulation. However, a qualitative agreement between simulation and experiment is observed. The differences can be attributed to multiple factors; hardware imperfections and model simplifications are present but were not identified explicitly.

Importantly, the critical misalignments can be obtained without using complex simulations. The values obtained from the buckling analysis method compare well with multibody simulations. These misalignments can be used to determine the manufacturing tolerances of a mechanism. The approach outlined in this article can be adapted to fit other types of compliant mechanisms.

## Acknowledgement

We would like to thank Leo Tiemersma for building the experimental setup. We would also like to thank Axel Lok at the University of Twente and Abhilash Chandrashekar and Dennis de Klerk at Delft, University of Technology for helping us with the modal measurement setup.

## References

[1] Blanding DL. Exact constraint: machine design using kinematic principles. 1st ed. New York: ASME Press; 1999.
[2] Hale LC. Principles and techniques for designing precision machines PhD. thesis Livermore CA: Lawrence Livermore National Laboratory; 1999.
[3] Howell LL. Compliant mechanisms. 1st ed. New York: Wiley; 2001.
[4] Haringx JA. The cross-spring pivot as a constructional element. Appl Sci Res 1949;1(1):313–32.
[5] Paros JM, Weisbord L. How to design flexure hinges. Mach Des November 1965:151–6.
[6] Smith ST. Flexures: elements of elastic mechanisms. 1st ed. London: Taylor and Francis; 2000.
[7] Hopkins JB, Culpepper ML. Synthesis of multi-degree of freedom, parallel flexure system concepts via freedom and constraint topology (FACT)Part I: Principles. Precis Eng 2010;34(4):259–70.
[8] Awtar S, Shimotsu K, Sen S. Elastic averaging in flexure mechanisms: a three-beam parallelogram flexure case study. J Mech Robot 2010;2(4):041006.
[9] Awtar S, Slocum A, Sevincer E. Characteristics of beam-based flexure modules. J Mech Des 2006;129(6):625–39.
[10] Brouwer DM, Folkersma G, Boer SE, Aarts RGKM. Exact constraint design of a two-degree of freedom flexure-based mechanism. J Mech Robot 2013;5(4):041011.
[11] Meijaard JP, Brouwer DM, Jonker JB. Analytical and experimental investigation of a parallel leaf spring guidance. Multibody Syst Dyn 2010;23(1):77–97.
[12] Nijenhuis M, Brouwer DM. Stiffness consequences of misalignments in a over-constrained flexure design. Proceedings of the 31st ASPE Annual Meeting 2016. Portland, OR, USA: American Society of Precision Engineering; 2016. p. 21–5.
[13] Grübler M. Allgemeine eigenschaften der zwangläufigen ebenen kinematischen ketten. Civilingenieur 1883;29:167–200.
[14] Brouwer DM, Boer SE, Meijaard JP, Aarts RGKM. Optimization of release locations for small self-stress large stiffness flexure mechanisms. Mech Mach Theory 2013;64:230–50.
[15] Lambert P. Parallel robots with configurable platforms Ph.D. thesis Delft University of Technology; 2013. https://doi.org/10.4233/uuid:ae07884d-52e2-4802-bc3f-fd298afe7e36.
[16] Timoshenko SP, Gere JM. Theory of elastic stability. 2nd New York: McGraw-Hill; 1961.
[17] Soemers HJMR. Design principles for precision mechanisms. Enschede: T-Pointprint; 2010.
[18] Gere JM. Mechanics of materials. 6th Belmont: Brooks/Cole; 2004.
[19] Selig JM. Geometric fundamentals of robotics. 2nd ed. Springer-Verlag New York Inc; 2005. In press.
[20] Jonker JB, Meijaard JP. SPACAR — computer program for dynamic analysis of flexible spatial mechanisms and manipulators. Multibody systems handbook. Springer Berlin Heidelberg; 1990. p. 123–43.
[21] Meijaard JP. Refinements of classical beam theory for beams with a large aspect ratio of their cross-sections. In: Kovács SG, Tóth A, editors. IUTAM Symposium on Dynamics Modeling and Interaction Control in Virtual and Real Environments. Dordrecht: Springer Netherlands; 2011. p. 285–92. IUTAM Bookseries, 30.
[22] Wijma W, Boer SE, Aarts RGKM, Brouwer DM, Hakvoort WBJ. Modal measurements and model corrections of a large stroke compliant mechanism. Arch Mech Eng 2014;61(2):347–66.